



HAL
open science

Variability of subtidal flow in a narrow meandering stratified estuary

Sophie Defontaine, Régis Walther, Damien Sous

► **To cite this version:**

Sophie Defontaine, Régis Walther, Damien Sous. Variability of subtidal flow in a narrow meandering stratified estuary. *Estuarine, Coastal and Shelf Science*, 2022, 266, 10.1016/j.ecss.2021.107716 . insu-03668108

HAL Id: insu-03668108

<https://insu.hal.science/insu-03668108>

Submitted on 22 Jul 2024

HAL is a multi-disciplinary open access archive for the deposit and dissemination of scientific research documents, whether they are published or not. The documents may come from teaching and research institutions in France or abroad, or from public or private research centers.

L'archive ouverte pluridisciplinaire **HAL**, est destinée au dépôt et à la diffusion de documents scientifiques de niveau recherche, publiés ou non, émanant des établissements d'enseignement et de recherche français ou étrangers, des laboratoires publics ou privés.



Distributed under a Creative Commons Attribution - NonCommercial 4.0 International License

Variability of subtidal flow in a narrow meandering stratified estuary

Sophie Defontaine^(a), Régis Walther^(b), Damien Sous^(c,d)

^(a) CNRS / Univ. Pau & Pays Adour / E2S UPPA, Laboratoire de Mathématiques et de leurs Applications de Pau - Fédération MIRA, UMR5142 64000, Pau, France

^(b) Artelia, 6 rue de Lorraine · 38130 Echirolles · France

^(c) Université de Toulon, Aix Marseille Université, CNRS, IRD, Mediterranean Institute of Oceanography (MIO), La Garde, France

^(d) Univ. Pau & Pays Adour / E2S UPPA, Laboratoire des Sciences de l'Ingénieur Appliquées à la Mécanique et au Génie Electrique (SIAME) - MIRA, EA4581, 64600, Anglet, France

Abstract

A 3D numerical model was set up to investigate the spatial and temporal variations of subtidal circulation in a narrow meandering stratified estuary: the Adour Estuary (France). The hydrodynamic model was validated with field data and reproduced satisfactorily tide, current and salinity observations. The results highlighted a fortnightly switch in the residual flow structure and a variation in residual circulation intensity between low and high river discharge conditions. During neap tides an exchange flow was observed as the baroclinicity dominated the residual circulation. During spring tides, the advection and barotropic pressure gradient drove the subtidal flow and an outflow over the whole water column took place. Residual flows were twice as high during high river discharge as during low river discharge. Secondary cross-channel residual circulation was driven by the estuarine morphology and the along-channel residual circulation. A secondary circulation cell was observed when a density-driven exchange flow occurred (neap tide). The meanders induced a variation of the sense of rotation of the circulation cell. A constriction of the channel has been shown to strengthen the residual circulation by flow conservation. Finally, we observed that the freshwater Froude number and the Mixing number (Geyer and MacCready, 2014) were able to distinguish residual flow pattern between idealized simulation cases.

Keywords: 3D numerical modelling, stratified estuary, subtidal flow, fortnightly switch, exchange flow, meanders

28 1. Introduction

29 Understanding and predicting circulation in estuaries is of primary importance in maintaining
30 and improving water quality and the health of estuarine and coastal ecosystems. A major chal-
31 lenge resides in the complexity and variability of the forcing mechanisms applied to each estuarine
32 system, including tidal currents, turbulent mixing, river flow, density gradients and bathymetry. A
33 classical strategy is to tidally-average flow properties, allowing common and differentiating features
34 to emerge. Since Pritchard's pioneering study (Pritchard, 1952), the tidally-averaged circulation,
35 also named subtidal flow or residual circulation, has been extensively documented as it determines
36 the long-term transport of suspended and dissolved material such as salt, sediments, pollutants,
37 nutrients, and larvae (see the review of Geyer and MacCready (2014)).

38 The most prominent feature revealed by Pritchard (1952) was named "gravitational circulation".
39 It is primarily driven by the baroclinic pressure gradient and characterised by an inflow motion of
40 the deeper salty layer of the water column while the overlying fresh layer flows out of the estuary,
41 leading to the so-called exchange flow. However, the residual circulation may show significant vari-
42 ations around this conceptual scheme, arising from the space- and time-varying relative importance
43 and interactions between major drivers such as tidal currents, density field, river flow, wind and
44 bathymetry (Geyer and MacCready, 2014). In particular, in tidally energetic estuaries, the relative
45 importance of each driver can alternate during the fortnightly cycle. When baroclinic pressure gra-
46 dients control subtidal flows, the resulting exchange flow is strong and further exacerbated in neap
47 tides due to low vertical mixing. By contrast, during spring tides, tidal stress can become dominant
48 and a strong outflow over the entire water column can develop. On a longer time scale, seasonal
49 variations of wind or river flow may also influence the residual circulation (Wong and Garvine, 1984;
50 Chawla et al., 2008). In addition, the structure of the residual circulation may also vary with the
51 estuarine morphology (Chant et al., 2018; Li and O'Donnell, 2005; Valle-Levinson, 2008).

52 In order to study estuarine circulation and its fortnightly variability, several estuaries worldwide
53 have been documented experimentally (Caceres et al., 2003; Geyer and Cannon, 1982; Noble et al.,
54 1996; Tenorio-Fernandez et al., 2018; Valle-Levinson et al., 2009; Valle-Levinson and Schettini,
55 2016). From the in-situ observations, the overall magnitude and structure of subtidal flows were
56 derived, as well as the first understanding of the driving mechanisms and circulation components
57 (Chatwin, 1976; Geyer et al., 2000; Geyer and MacCready, 2014; Hansen and Rattray, 1966; Wong,
58 1994). While necessary, these experimental studies are intrinsically limited in time and space,
59 with observations at only one or a few positions or transects for few days or weeks. To achieve
60 a comprehensive space- and time-resolved understanding of the estuarine circulation, numerical
61 models can be powerful tools once properly calibrated and validated. They are extensively used
62 in estuarine physics to complement experimental data, see e.g. (Alahmed et al., 2021; Burchard
63 and Hetland, 2010; Burchard et al., 2011; Jay and Smith, 1990; Ralston et al., 2008; Scully et al.,
64 2009). A fundamental step in the research effort has been to work on idealised simulations with
65 constant estuarine geometries (rectangular, triangular or Gaussian shapes) which provided general
66 insight as to the magnitude and the structure of residual flows and as to the relative importance
67 of the driving mechanisms. The classical understanding of the estuarine circulation as dominated
68 by a balance between the horizontal pressure gradient and the vertical stress divergence has been
69 rethought. The importance of other mechanisms such as advection (Lerczak and Geyer, 2004; Scully
70 et al., 2009), tidal non-linearities (Ross et al., 2017), tidal straining (Burchard and Hetland, 2010),

71 and wind (Wong, 1994) in affecting the residual flows were demonstrated. The lateral circulation,
72 which is generally neglected compared to the along-channel circulation, has been shown to be a
73 dominant forcing of the residual circulation under weakly stratified conditions, i.e. even larger
74 than the pressure gradient, making the exchange flow stronger than expected (Lerczak and Geyer,
75 2004). Idealised simulations also demonstrated that estuarine morphology can affect the structure
76 of residual circulation (Valle-Levinson, 2008; Wong, 1994). In similar conditions, a rectangular
77 shaped cross-section induced a "classical" exchange flow with inflow at the bottom and outflow
78 near the surface, while a triangular cross-section produced an inflow in the centre of the channel
79 and outflow over the shoals. In addition, channel curvature appeared to be able to control the
80 lateral circulation (Kim and Voulgaris, 2008; Chant, 2002). The relative importance of such forcing
81 may also vary spatially, i.e. in the along-channel direction (Chant and Wilson, 1997).

82 More recently, realistic simulations have demonstrated that, inside a given estuary, the structure
83 and the relative importance of the driving mechanisms in residual flows vary both temporally and
84 spatially. For instance, in the Gironde estuary the predominant driver of the residual flow was shown
85 to vary from neap to spring tide, with density-driven flow and advection-driven flow dominating
86 the residual circulation during neap and spring tides, respectively. Morphological changes were
87 also responsible for the structural modification of residual flows from the mouth to the head due
88 to the convergence of the estuary and the modification of the cross-section shape (from triangular
89 to rectangular shape) (Alahmed et al., 2021). These results emphasise the need to complement
90 idealised approaches with more realistic and more complex simulations.

91 The aim of the present study is to investigate the spatial and temporal variability of the sub-
92 tidal flow and the secondary circulation in a tidally-energetic meandering estuary. Special focus is
93 given to the switch of major forcing under different hydrological conditions (fortnightly cycle and
94 seasonal discharge variations). This study is based on a site which combines the challenges of a
95 particularly narrow meandering morphology and a highly-variable salinity structure referred to as
96 time-dependent salt-wedge: Adour Estuary. The characterisation of the residual circulation was
97 carried out with 3D numerical simulations carefully validated with field measurements. Particular
98 attention has been paid to a possible switch in residual flow structure, expected to occur over the
99 fortnightly cycle based on previous field observations (Defontaine et al., 2019).

100 **2. Material and methods**

101 *2.1. Study site*

102 The Adour estuary is a winding narrow man-engineered estuary connected to the southwestern
103 Bay of Biscay (SW of France). The estuary morphology is fully artificial due to successive engineer-
104 ing works carried out several decades ago in order to stabilise the river mouth position, to favour
105 sediment flushing by ebbing currents and to facilitate navigation in the harbour. The first 6 km
106 from the mouth of the estuary compose Bayonne harbour and are almost completely channelled
107 by embankments. In this section, the channel width ranges from 150 m to 400 m while the depth
108 is maintained by dredging to about 10 m depth along the dock. A 700 m-long jetty protects the
109 estuary from Atlantic swells by lessening the wave energy by about 85 % (Bellafont et al., 2018).

110 The estuary is exposed to a semidiurnal mesotidal forcing with a mean tidal range of 2.5 m.
111 M2, N2, S2 and K2 are the major components of the tidal signal with an amplitude of 1.22 m, 0.42

112 m, 0.25 m and 0.12 m respectively. Those amplitudes decrease as the tidal wave propagates into
 113 the estuary. The main harmonics at Urt village (22km from the mouth of the estuary) are M2, S2,
 114 N2 and MSF, with an amplitude of 0.92 m, 0.27 m, 0.18 m and 0.11 m (Defontaine et al., 2019).
 115 The limit of salt intrusion is Urt Village ca. 22 km from the mouth of the estuary, while the tidal
 116 influence is limited by a weir ca. 70 km from the mouth.

117 Defontaine et al. (2019) have documented the saline structure and its variations using field
 118 measurements under different hydrological conditions, inside the lower Adour Estuary. Seasonal
 119 variations in river flow and fortnightly variations in tidal range modify the density stratification
 120 inside the estuary from salt-wedge to partially mixed regimes. Stratification is strengthened during
 121 the wet season by a stronger river flow that can reach more than $3000 \text{ m}^3 \cdot \text{s}^{-1}$ during spring freshets.
 122 During the dry season (ca. $80 \text{ m}^3 \cdot \text{s}^{-1}$), spring tides generate turbulent mixing especially during
 123 the falling tide, while neap tides display a quasi-static salt-wedge. Overall, the Adour Estuary is
 124 classified as time-dependent salt-wedge estuary.

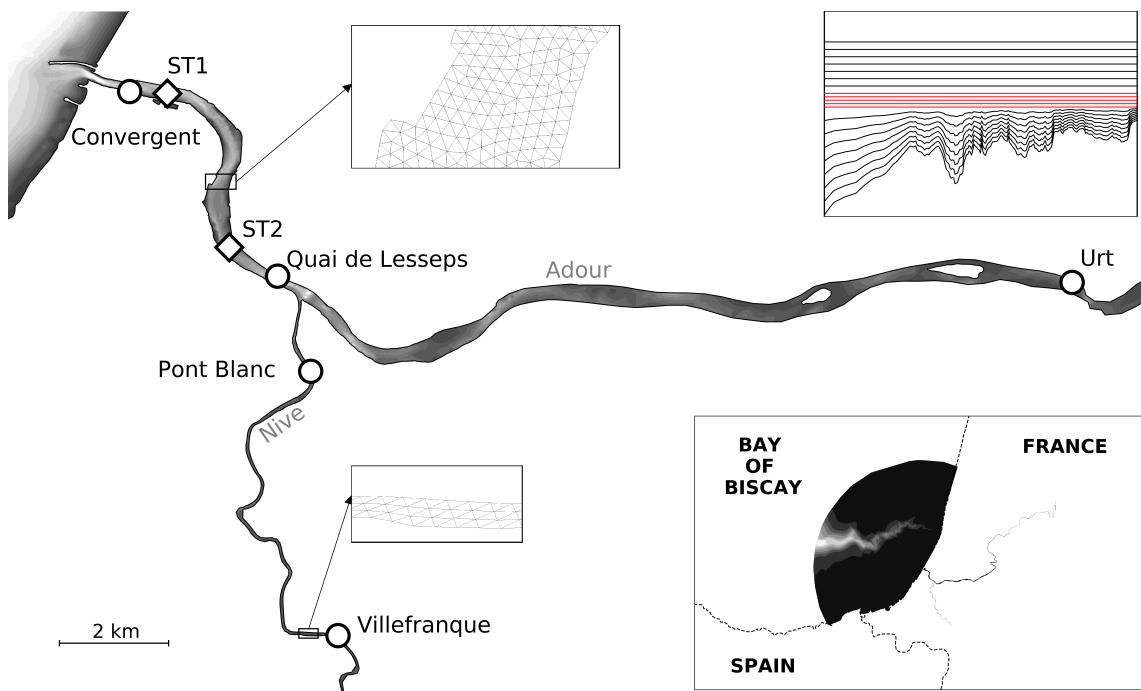


Figure 1: Study site. The total estuarine and coastal areas covered by the numerical model are depicted on the bottom right corner while the large schema provides a zoomed view of the main area of interest. Two examples of the regular and irregular mesh implemented in the estuary are displayed in the arrowed frames. The white dots indicate the locations of the tidal gauges and the white squares represent the measurement stations ST1 and ST2 used for the model validation. The vertical distribution of the layers is presented in the top right corner.

125 2.2. Numerical model

126 A numerical model of the Adour River Estuary and the Basque Coast was developed with
 127 TELEMAC3D from the open TELEMAC-MASCARET system. This finite element software solves
 128 the free-surface flow Navier-Stokes equations (Hervouet, 2007). The Boussinesq approximation on
 129 the density was taken into account in the momentum equations and the pressure was assumed
 130 to be hydrostatic. Turbulent mixing of momentum and mass were estimated using a standard
 131 $k - \omega$ closure model (Wilcox, 1988; Peng et al., 1996). The water density was estimated based on

132 salinity field only (Hervouet, 2007), which overwhelmingly dominates the effect of temperature in
133 the present context. A classical transport equation (advection/diffusion) was used to compute the
134 dispersion of salinity.

135 The model was implemented on the whole estuary and the adjacent coastal area (see Figure 1).
136 The computation grid covered the ocean up to 40 km from the estuary mouth and 70 km upstream
137 into the Adour River and 25 km into the Nive River. The mesh is composed of irregular triangular
138 elements. A finer resolution was used in the lower Adour Estuary (i.e. the area of interest) with cells
139 of 30 m, while the largest cells of 2 km were located in the external maritime boundary (Fig. 1).
140 This 2D mesh basis was interpolated on the latest available bathymetry data and it was projected
141 on each vertical layer, generating prisms with quadrilateral sides. The vertical axis was split into 20
142 layers spaced using a double sigma transform, i.e. we prescribed a constant elevation for 5 planes
143 around the mid-depth, then the planes between the bed and the deepest fixed plane were evenly
144 spaced; the same was done between the upper fixed plane and the free surface (Fig. 1). The five
145 fixed planes maintained a good vertical resolution at the pycnocline elevation in the lower estuary
146 under all conditions. In the area of interest, the water column layers were about 0.5 m thick.

147 For *realistic simulations*, mainly used for the calibration and validation phases, a real tide was
148 imposed at each node of the maritime boundary. It was calculated as the sum of 11 harmonic
149 components interpolated from tidal charts covering the Atlantic Ocean. This global solution for
150 tide, named TPXO, was developed by Oregon State University (OSU). At the upstream limit of
151 the Adour River and the Nive River, a hourly river flow was forced based on data collected by the
152 Adour-Garonne Water Agency (see Section 2.3).

153 For *idealized simulations* used for the analysis of the residual circulation, constant values of
154 tidal range and river input were prescribed on open boundaries. Four simulations were carried out
155 under different hydrological conditions: low river discharge ($Q_{Adour} = 95 \text{ m}^3 \cdot \text{s}^{-1}$ and $Q_{Nive} = 10$
156 $\text{m}^3 \cdot \text{s}^{-1}$) and high river discharge ($Q_{Adour} = 1150 \text{ m}^3 \cdot \text{s}^{-1}$ and $Q_{Nive} = 270 \text{ m}^3 \cdot \text{s}^{-1}$) for both a
157 neap (1.2 m) and a spring tide (4.4 m). The simulations are named following the forcing conditions,
158 LD/HD referring to low/high river discharge and ST/NT referring to spring/neap tide conditions,
159 respectively.

160 Both jetties located at the entrance of the estuary reduce the offshore wave energy by a factor
161 of 85% (Bellafont et al., 2018), therefore the wave effect is expected to be weak inside the estuary.
162 The low wind exposure of the estuary associated with a reduced fetch due to the S shape of the
163 lower estuary suggests low influence of the wind on the estuarine dynamics. Therefore, no wind or
164 wave forcing was considered in the present computations.

165 2.3. Field data collection

166 The model validation (*realistic simulations*) was based on three field campaigns carried out
167 between September 2017 and September 2018 (Defontaine, 2019; Defontaine et al., 2019). First,
168 two bottom-moored pyramidal frames were deployed at stations ST1 and ST2 (white squares in
169 Figure 1) during one month in September 2017. Both frames were equipped with ADCP. Velocity
170 profiles were recorded at 4 Hz during 5 min every 15 min. During this field campaign, the tidal
171 range varied between 1.2 m and 3.8 m and the Adour River and Nive River discharge ranged
172 from $74.6 \text{ m}^3 \cdot \text{s}^{-1}$ to $290 \text{ m}^3 \cdot \text{s}^{-1}$ and from $8.1 \text{ m}^3 \cdot \text{s}^{-1}$ to $81.3 \text{ m}^3 \cdot \text{s}^{-1}$, respectively. During the
173 second and third field campaigns, on June 12th and September 25th 2018, velocity, salinity and

174 temperature profiles were collected from an anchored boat at ST2 station. The reader is referred to
 175 Defontaine et al. (2019) for more details regarding the data collection and post-processing. During
 176 both experimentation the tidal amplitude was 3.2 m and the river flow was $1421 \text{ m}^3 \cdot \text{s}^{-1}$ in June
 177 and $103 \text{ m}^3 \cdot \text{s}^{-1}$ in September.

178 Hourly river discharge values from the Adour River and its tributaries were retrieved from the
 179 French Water Agency website (www.hydro.eaufrance.fr). The Adour River flow was approximated
 180 as the sum of river flows collected at the downstream Adour station and all the downstream tribu-
 181 taries except the Nive River. Water elevation data were available for five tidal gauge stations (grey
 182 dots in Figure 1) located along the Adour and the Nive Rivers : Convergent, Quai de Lesseps, Urt,
 183 Pont Blanc and Villefranque (www.datashom.fr).

184 2.4. Dynamic analysis

185 2.4.1. Along-channel momentum equation

186 Numerical results were used to evaluate the relative influence of each forcing term in the tidally-
 187 averaged momentum equation in the along-channel direction. In a right-handed coordinate system
 188 (x, y, z) where the along-channel x axis is landward-directed, the transverse y axis is directed towards
 189 the right bank and the vertical z axis is directed upward, the tidal average of the along-channel
 190 momentum balance is given by

$$191 \quad \overline{u \frac{\partial u}{\partial x}} + \overline{v \frac{\partial u}{\partial y}} + \overline{w \frac{\partial u}{\partial z}} + \frac{\overline{uv}}{R} = -g \frac{\partial \overline{\eta}}{\partial x} + \frac{g}{\rho} \int_z^n \frac{\partial \rho}{\partial x} dz + \frac{\partial (A_z \frac{\partial \overline{u}}{\partial z})}{\partial z} + f \overline{v} \quad (1)$$

192 where (u, v, w) are the velocity components in the (x, y, z) coordinate system, and g , ρ , η ,
 193 A_z , f and R are the gravity acceleration, the water density, the surface elevation, the vertical
 194 eddy viscosity, the Coriolis parameter, and the radius of the estuarine curvature respectively. The
 195 overbar indicates a tidally average value. On the left side of Eq. (1), the three first terms are
 196 respectively the longitudinal advection, the lateral advection and the vertical advection, while the
 197 fourth term represents the estuarine curvature. On the right side of Eq. (1), the first two terms are
 198 the barotropic and the baroclinic pressure gradients. The third term is the stress divergence. The
 199 fourth term is the Coriolis force.

200 2.4.2. Ekman and Kelvin numbers

201 In order to investigate the influence of the bathymetry (width and depth) in the density-driven
 202 exchange flow pattern, two dimensionless numbers were estimated: the Kelvin and Ekman numbers.
 203 The Ekman number $Ek = A_z / (fH^2)$ compares frictional effect to Coriolis forcing, where H is a
 204 typical depth scaling. At low Ek (< 0.01), frictional effect is weak and the Coriolis effect becomes
 205 prominent, while at high Ek the Coriolis effect becomes negligible when compared to the friction
 206 force.

207 The Kelvin number $Ke = B/R_i$ evaluates the capacity of the Earth's rotation to affect the
 208 density-induced exchange flow in relation to the channel width B , where R_i is the internal Rossby
 209 radius. The internal Rossby radius is estimated as $R_i = \sqrt{g'h}/f$, where $g' = g\Delta\rho/\rho_0$ is the reduced
 210 gravity. If the channel width is wider than the Rossby radius ($Ke > 1$), rotation due to the Coriolis
 211 effect is assumed to be predominant.

212 3. Model calibration and validation

213 3.1. Hydrodynamics

214 The model was calibrated by adjusting the bottom friction coefficient to reproduce tidal propa-
215 gation into the estuary. The water elevations measured at 5 tidal gauges along the Adour River and
216 the Nive River were compared to simulation results (Fig. 2). The best fit between simulations and
217 observations was found for a combination of Nikuradse and Strickler approaches for bed friction.
218 The Nikuradse law for friction was applied on the lower part of the estuary, i.e. our area of interest
219 with high spatial resolution. This representation of the bed friction is more appropriate for highly
220 resolved 3D modelling, as it is related to the bottom velocity. Furthermore, in the area of interest
221 during the rising tide a two-layer flow develops, where the bottom velocity is oppositely directed
222 to the depth averaged velocity. However, the Strickler formulation is more appropriate for an area
223 with low spatial resolution, as it is based on the depth averaged velocity. Therefore, the Strickler
224 formulation was applied to the upstream part of both rivers. The friction coefficient varied spatially
225 in the numerical model. In the upper part of the rivers, unrealistic values of friction coefficient were
226 used to ensure the damping of the tidal wave before the river boundaries. The resulting simulated
227 water level showed a good agreement with measurements (Fig. 2), with a Root Mean Square Error
228 between measured and simulated water levels ranging from 6 to 14 cm over the studied area.

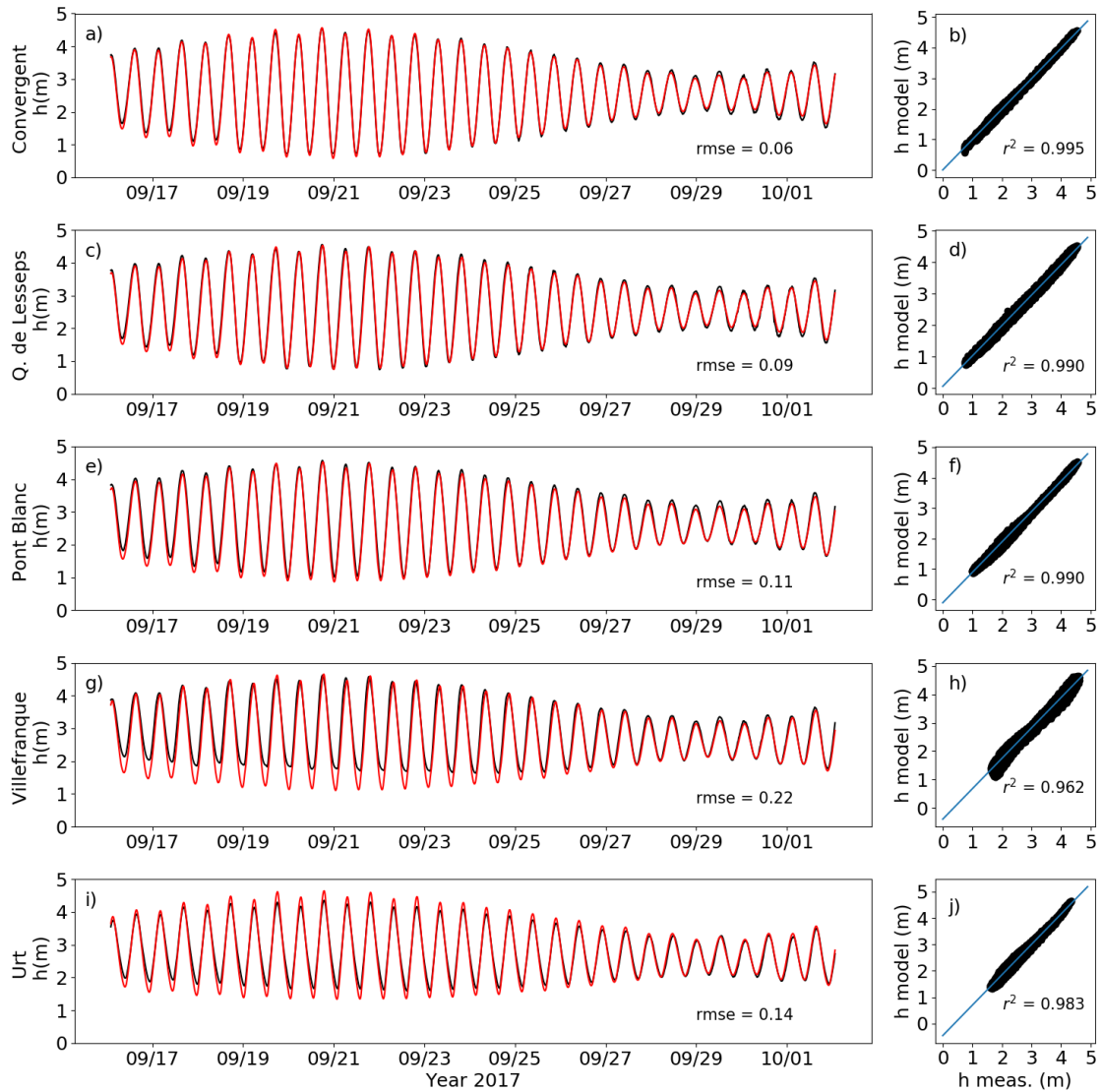


Figure 2: Simulated (red) and measured (black) water elevations at: a) Convergent, c) Quai de Lesseps, e) Pont Blanc, g) Villefranque and i) Urt, with the value of the root mean square error in meters. Linear regressions of measured against simulated water elevations with the r^2 values (b), (d), (f), (h) and (j)).

229 Further validation was performed on Eulerian velocity measurements based on two data sets
 230 of bottom-moored ADCPs deployed during one month in September 2017 at ST1 and ST2 (Fig.
 231 1). Velocities were estimated one meter below the surface and two meters above the bed. The
 232 numerical results presented in Figure 3 again show a very satisfactory agreement with field data.
 233 The Root Mean Square Error on velocities ranged from 10 to 21 $cm.s^{-1}$ in the studied area (Fig.
 234 3).

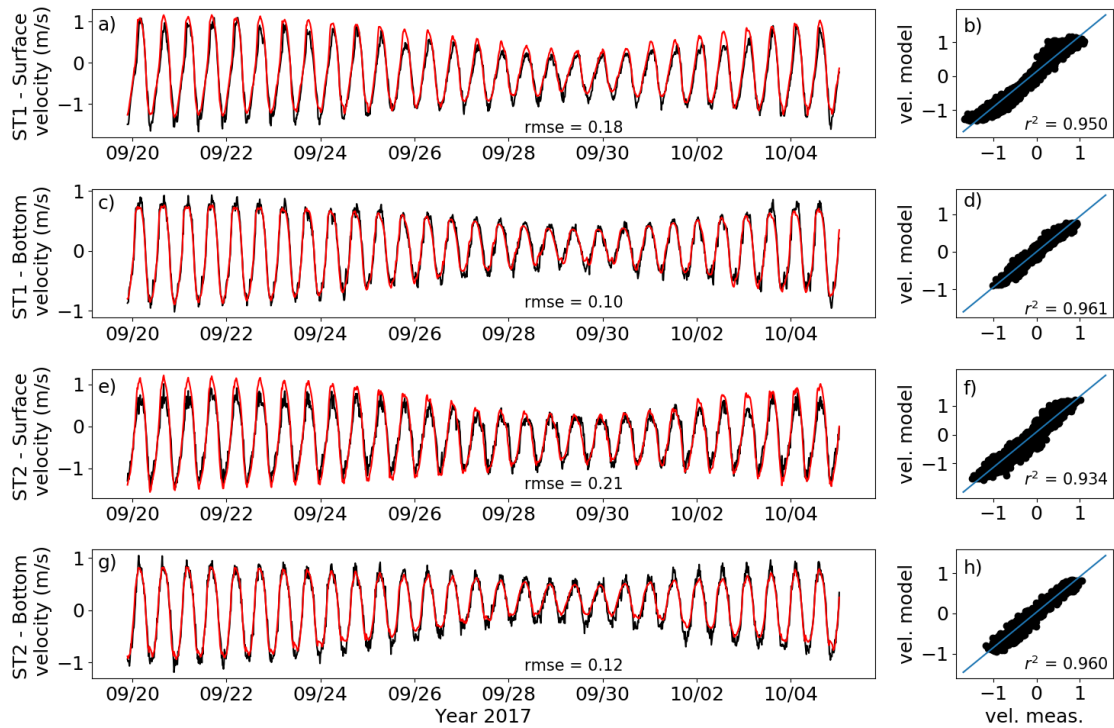


Figure 3: Simulated (red) and measured (black) along-channel velocities at ST1 and ST2 stations, with the value of the root mean square error in meters per second. Positive values denote inflow. The surface velocity corresponds to the velocity measured one meter below the surface and the bottom velocity two meters above the bed. Linear regressions of measured against simulated velocities with the r^2 values (b), (d), (f) and (h)).

235 *3.2. Density structure*

236 While the density stratification is challenging to properly reproduce with numerical models, it
 237 is a key parameter of the estuarine dynamics. The numerical fields of density were validated with
 238 vertical profiles of density collected during 10 consecutive hours in June and September 2018 at
 239 ST2 (Defontaine et al., 2019). Both experiments were conducted under similar tidal range but
 240 with a much stronger river flow in June, leading to very different stratification patterns. Figure
 241 4 depicts time series of measured and simulated surface (1m below the surface) and bottom (2m
 242 above the bed) salinity, together with linear regressions. A satisfactory agreement was obtained,
 243 confirming the validity of the turbulence model in reproducing the turbulent mixing over time- and
 244 space-varying density field. The Root Mean Square error remained lower than 5.

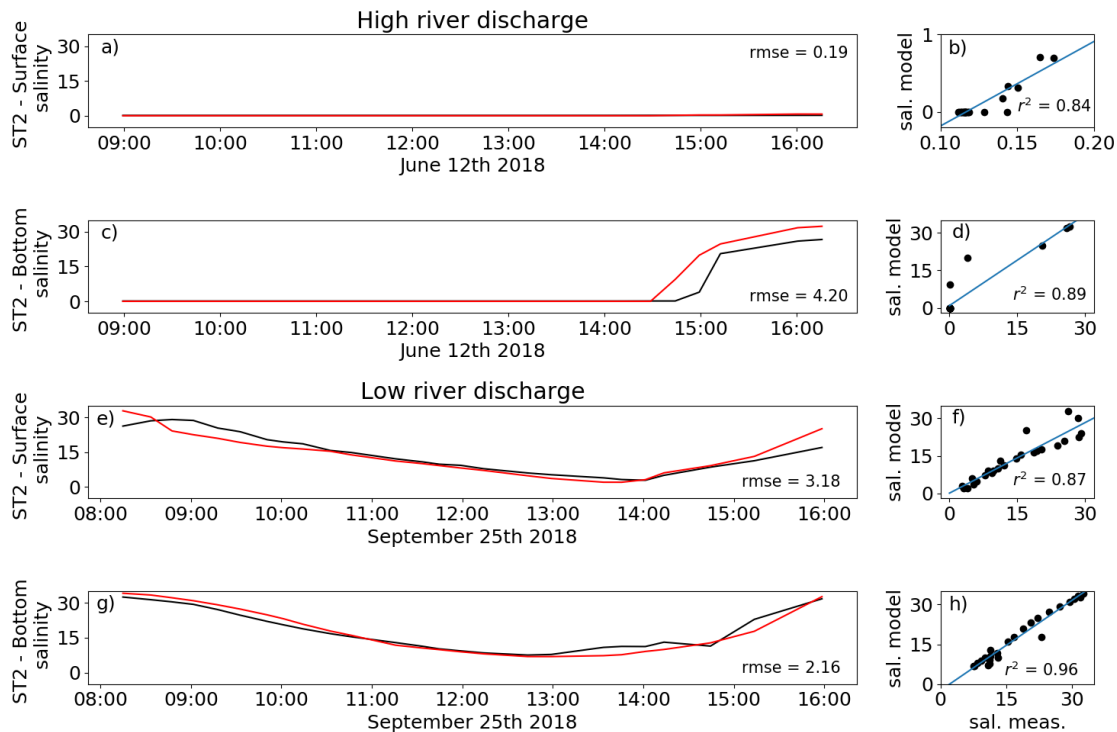


Figure 4: Simulated (red) and measured (black) salinity at ST2 station under high and low river discharge conditions (June 12th and September 25th 2018, respectively), with the value of the root mean square error. The surface salinity corresponds to the salinity measured one meter below the surface and the bottom salinity one meter above the bed. Linear regressions of measured against simulated salinity with the r^2 values (b, d), f) and h)).

245 3.3. Residual circulation

246 In order to evaluate the ability of the numerical model to reproduce the fortnightly evolution of
 247 the residual circulation in the lower estuary, a realistic simulation covering a three-week period in
 248 September 2017 was run and results were compared to ADCP data at ST2. Figure 5 depicts the
 249 time series of tidally-averaged velocity profiles at ST2 station under low discharge conditions, with
 250 a comparison of bottom-moored ADCP measurements (Fig. 5a) and numerical (Fig. 5b) results.
 251 First the good agreement between simulation and observation with a $rmse$ of $9\text{ cm}\cdot\text{s}^{-1}$ confirms
 252 the relevancy of the numerical strategy. A fortnightly switch is clearly observed in the structure
 253 of the residual flow and it is properly reproduced by the numerical model. During neap tides, the
 254 residual flow is vertically sheared with an inflow on the bottom of the water column and outflow
 255 on the surface. The resulting exchange flow periods are highlighted with grey patches in Figure
 256 5. By contrast, spring tides display an outflow in the whole water column. In September, 10th
 257 a small flood event increased the river flow from a typical value of about $100\text{ m}^3/\text{s}$ to more than
 258 $400\text{ m}^3/\text{s}$. This enhanced freshwater input prevented the salt-wedge from reaching the ST2 station
 259 and therefore resulted in a delay in the exchange flow development before September, 15 at ST2
 260 station, observed in both numerical and field data. However, a overestimation of the residual can
 261 be observed between September, 24 and October, 9.

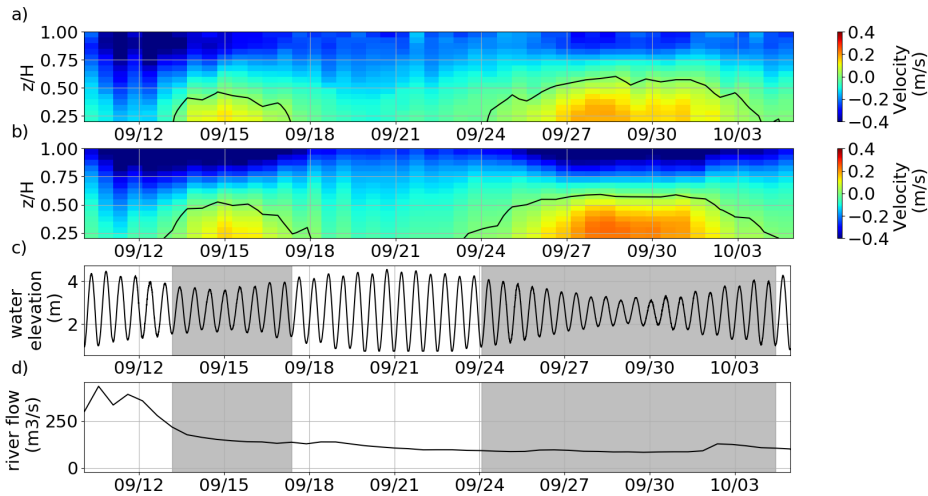


Figure 5: Timeseries of (a) observed tidally-averaged along-channel velocity profiles, (b) simulated tidally-averaged along-channel velocity profiles at ST2 station on September 2017 (dry season). Positive values denote inflow. The ratio z/H represents a dimensionless height, with z the distance to the bottom and H the water column depth. The black line represents the zero velocity value. (c) Timeseries of water elevation in meter. Grey areas correspond to periods when an exchange flow was observed.

262 4. Results

263 The results presented in the following subsections were produced by the means of four idealized
 264 numerical simulations with contrasted hydrological conditions, as described in Section 2.2. The
 265 influence of tidal and riverine forcings on the residual along-channel flow and secondary circulation
 266 are described in the following subsections. The residual flow analysis is based on a series of sections
 267 placed every two kilometres over twenty two kilometres, from the mouth of the estuary (see Figure
 268 6). The velocity data are projected into a local coordinate system with the x axis directed along the
 269 channel with positive values for an inflow, the y axis directed laterally towards the right bank, and
 270 the z axis directed upward. The descriptive terms left bank and right bank refer to the perspective
 271 of an observer looking downstream/seaward.

272 4.1. Along-channel residual flows

273 Figure 6 depicts tidally-averaged velocity profiles of the along-channel component extracted at
 274 successive points in the thalweg along the estuary to analyse the spatial evolution of residual flows
 275 along the estuary under the four contrasted scenarios. Contour lines represent the tidally-averaged
 276 density field while the tidally-averaged along-channel velocity is depicted in colour levels.

277 4.1.1. Descriptive overview

278 During neap tides, an exchange with outflow at the surface and inflow beneath was produced in
 279 the thalweg until the saline intrusion limit, upward of which the velocity profiles display vertically-
 280 sheared profiles, under both river flow conditions (Fig. 6b and c). The river discharge strongly
 281 affected the salinity intrusion : at low discharge the salinity intrusion was 16 km, while at high

282 river discharge it was limited to 2 km. The horizontal stratification was therefore higher in the
283 high discharge scenario ($\frac{\partial S_{bottom}}{\partial x} \sim 6.25 \text{ km}^{-1}$) than in the low discharge scenario ($\frac{\partial S_{bottom}}{\partial x} \sim 1.9$
284 km^{-1}). The river flow also influenced the vertical stratification with an increase of the vertical
285 salinity gradient with stronger river flow. As a consequence, the exchange flow during the high
286 river discharge scenario (Fig. 6 c) was almost twice as strong as the exchange flow during low river
287 discharge scenario. In low discharge conditions (Fig. 6 b), the thalweg exchange flow varied in
288 intensity along the estuary with flow reinforcement at 6 km, 10 km and 14 km. It may have been
289 influenced by the estuarine morphology, as the channel was narrower at 6 km, and the sections were
290 asymmetric at 10 km and 14 km (Fig. 8 and 9). The influence of the morphology will be discussed
291 in the following section.

292 During spring tides (Fig 6d-e), the residual circulation was characterised by a much weaker
293 exchange flow along the thalweg. In high river flow conditions, the residual flow consisted in a
294 general outflow of the water column. In low river flow conditions, the residual circulation is about
295 twice as weak as in high discharge conditions. A small exchange was observed near the entrance of
296 the estuary (0km) and at 14 km (Fig 6d), but the main trend is a nearly steady situation in the
297 lower half of the water column and a seaward residual flow in the upper half. The forcing responsible
298 for the localized exchange flows will be discussed below based on the quantitative analysis of the
299 forcing mechanisms. The river flow had a similar influence on the salinity pattern as during neap
300 tides, with greater horizontal and vertical gradients during high river flow. In low river discharge
301 scenario, the vertical stratification is very weak and the salinity intrusion length is 16 km.

302 It is interesting to notice that the overall saline intrusion was greater during neap tides than
303 during spring tides.

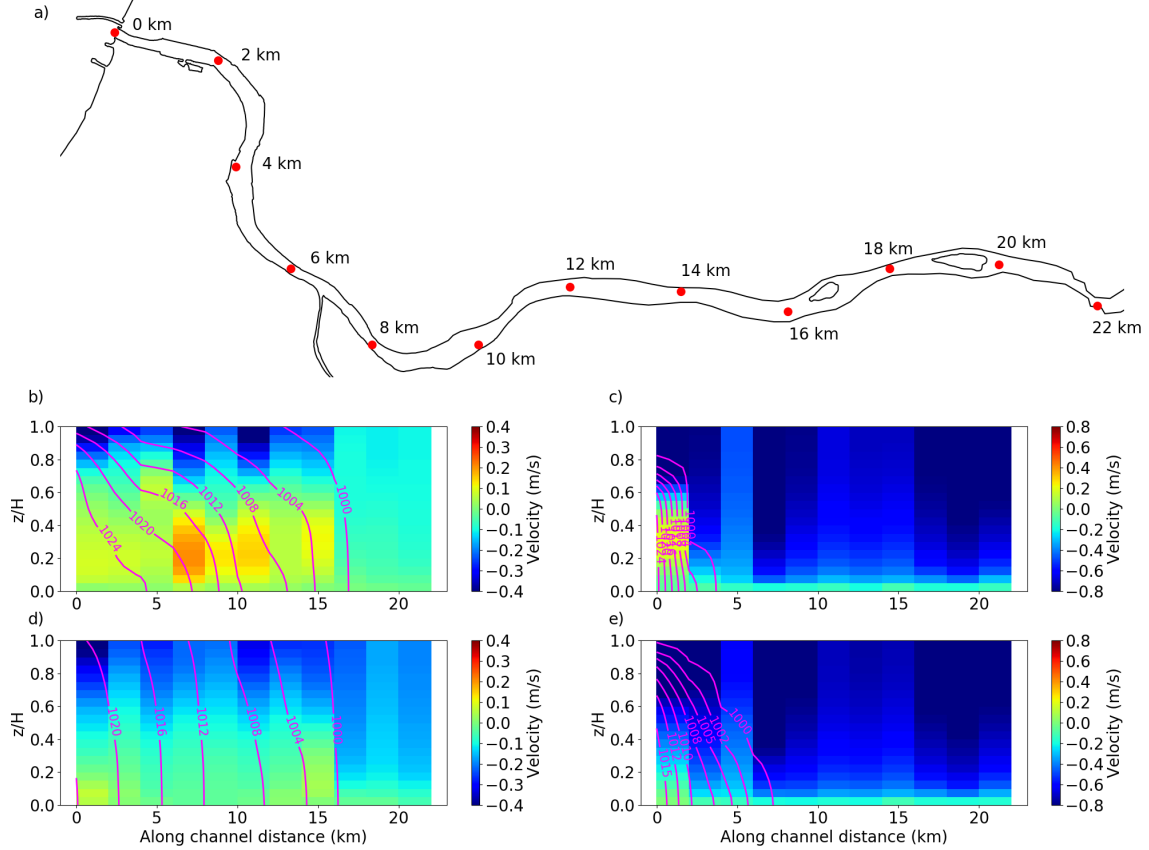


Figure 6: Variability of the tidally-averaged along-channel velocity for the four forcing conditions: b) Low discharge and neap tide, c) high discharge and neap tide, d) low discharge and spring tide, e) high discharge and spring tide. a) Locations where the data were extracted from the simulation results (red dots). Density (kg/m^3) contours are represented in magenta.

304 4.1.2. Forcing mechanisms

305 Figure 7 represents the along-channel variation of the different momentum fluxes governing
 306 the tidally-averaged along-channel momentum equation (see Eq. (1)) under the four hydrological
 307 conditions.

308 During neap tides and low river discharge (LDNT), the baroclinic and barotropic pressure
 309 gradients were the major forcing in the first 16 km of the estuary, i.e. where the exchange flow
 310 took place. The contributions of longitudinal and lateral/vertical advection terms were at least
 311 three times lower. Upstream, the advection term and the barotropic pressure gradient dominated
 312 the momentum balance. When river flow increased (HDNT), in the first 2 km of the estuary, the
 313 influence of baroclinic pressure gradient remained limited to the first 2 km of the estuary, again in
 314 relation to the exchange flow localisation. The 2-10 km balance was mainly governed by barotropic
 315 pressure gradient and advection terms, while from 10 km, the stress divergence term increased,
 316 likely related to the depth reduction.

317 The tidal range increase (LDST and HDST cases) led to an overall weaker contribution of the
 318 baroclinic pressure gradient and a stronger effect of advection terms. During spring tides (LDST),
 319 advection terms and barotropic pressure gradient were the major forcing, except at 14 km where
 320 baroclinic pressure gradient became equivalent to the longitudinal advection term and overcame the

321 others. This small dominance of the baroclinicity resulted in a localised exchange flow at 14km (Fig
 322 6d). Under high discharge (HDST), barotropic pressure gradients and advection terms dominated
 323 until 10 km where barotropic pressure term and stress divergence term alternatively governed the
 324 residual circulation.

325 In all scenarios, the centrifugal force due to the estuarine curvature was mainly negligible as
 326 well as the Coriolis force, except at 22 km where the centrifugal force overcame stress divergence
 327 forcing.

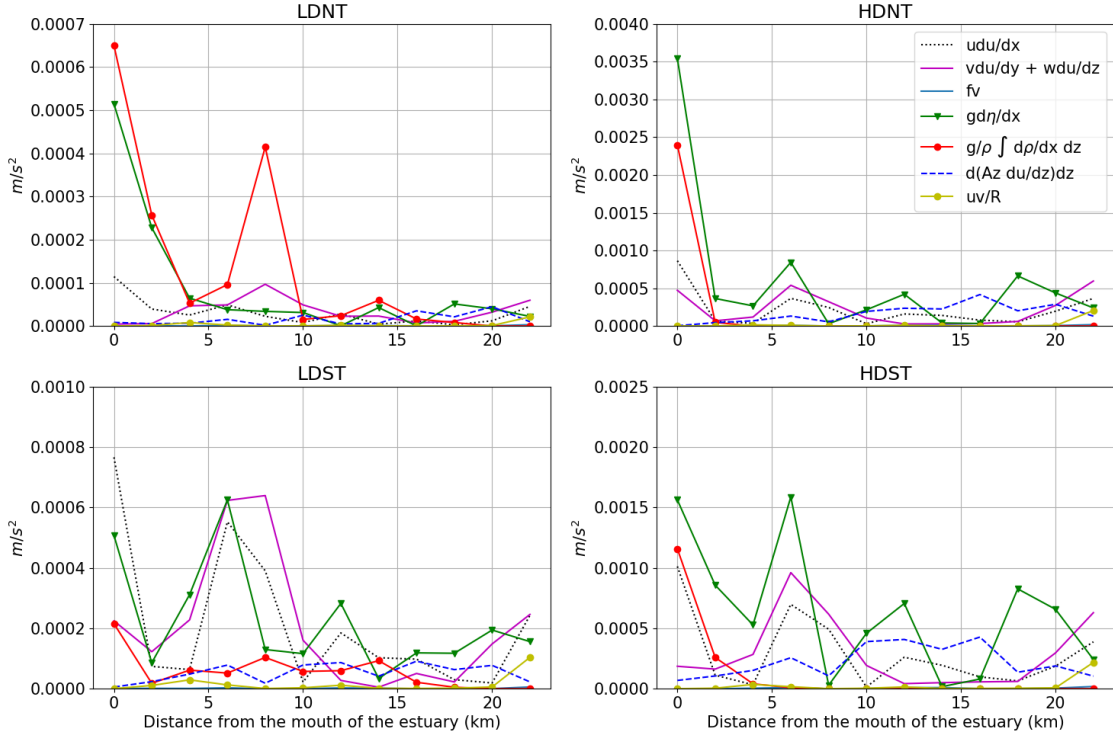


Figure 7: Along-channel variation of the area and tidally averaged terms (Eq. (1)) : longitudinal advection ($u\partial u/\partial x$), lateral and vertical advection ($v\partial u/\partial y + w\partial u/\partial z$), barotropic pressure gradient ($g\partial\eta/\partial x$), baroclinic pressure gradient ($g/\rho \int \partial\rho/\partial x dz$), stress divergence ($\partial(A_z \partial u/\partial z)/\partial z$), Coriolis (fv) and estuarine curvature (uv/R), for the four idealised simulations : low discharge and neap tide (LDNT), high discharge and neap tide (HDNT), low discharge and spring tide (LDST) and high discharge and spring tide (HDST).

328 4.1.3. Residual secondary circulation

329 The residual secondary circulation refers to the tidally-averaged lateral circulation, i.e. the
 330 tidally-averaged cross channel component of the velocity. The analysis was performed on 12 cross
 331 sections at the selected locations shown in Fig. 6 (red dots). Figures 8 and 9 depict the tidally-
 332 averaged along-channel velocity (colour levels in m/s), cross-channel velocity (white arrows) and
 333 salinity (pink contour lines).

334 A first general observation is that residual lateral velocities were significantly lower than their
 335 along-channel counterparts. In each case, tidally-averaged vertical velocities show magnitudes of
 336 less than 1 cm/s.

337 The numerical results highlighted that the residual secondary circulation mostly depends on
 338 the estuarine morphology and tidally-averaged longitudinal circulation. The estuarine morphology

339 affected the secondary residual circulation in two ways: by the presence of meanders and by the
340 presence of shoals. First, the meanders induced a variation of the direction of rotation of the flow
341 along the estuarine channel. At 2 km, a clockwise secondary circulation was produced under low
342 river flow (Fig. 8), while at 6 km a counterclockwise secondary circulation occurred under the
343 same river flow conditions. This results in a complex spiral-flow pattern along the estuary. At
344 both locations, the secondary circulation was reinforced during spring tide compared to neap tide.
345 Second, shoals affected the residual circulation by inducing stronger friction than in the thalweg.
346 For instance, at 10 km under spring tide and low river discharge (LDST), the shoal on the right
347 bank reduced strongly both along-channel and cross-channel circulations and induced a tilt of the
348 isopycnals in the thalweg and a longitudinal gradient of velocity (Fig. 8).

349 The residual secondary circulation was strongly related to the along-channel residual flow pat-
350 tern. At the mouth of the estuary, when an exchange flow was observed (i.e. under low river flow
351 and spring and neap tides, and under neap tide and high river discharge) a clockwise secondary
352 circulation occurred. However, when the along-channel circulation was an outflow throughout the
353 entire water column and the column was stratified (i.e. at high river flow and spring tide), it re-
354 sulted in a dual cell secondary circulation. At 4 km and 6 km under high discharge conditions,
355 the stronger along-channel advection tended to flatten the helical pattern, with a stronger lateral
356 circulation and a weaker vertical circulation.

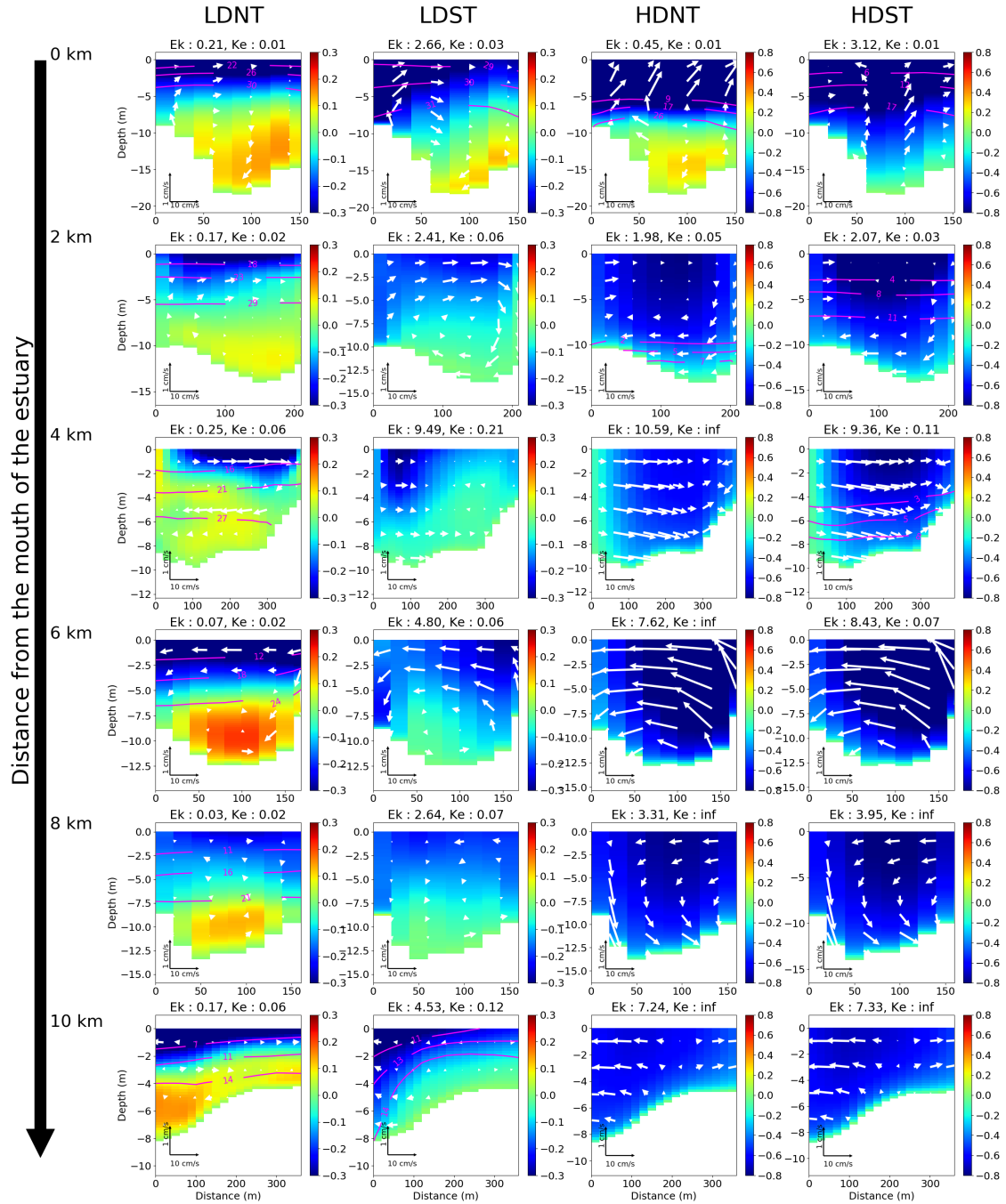


Figure 8: Cross-section of tidally-averaged along-channel velocity (in m/s on the colorbar) with positive values indicating inflow, tidally-averaged cross-channel velocity (white arrows) and tidally-averaged salinity (pink contour lines). From top to bottom cross-section correspond to the location of the red dot on Figure 6, respectively. To clarify the reading only one half of the cross-sections are represented on this figure (from 0 km to 10 km), the rest is presented in Figure 9. From left to right panel, each scenario is presented: low discharge and neap tide (LDNT), low discharge and spring tide (LDST), high discharge and neap tide (HDNT), and high discharge and spring tide (HDST). Tidally-averaged along-channel velocity colour scale is different for high discharge conditions than for low discharge conditions. The indicated Ekman (Ek) and Kelvin (Ke) numbers are discussed in section 5.1.

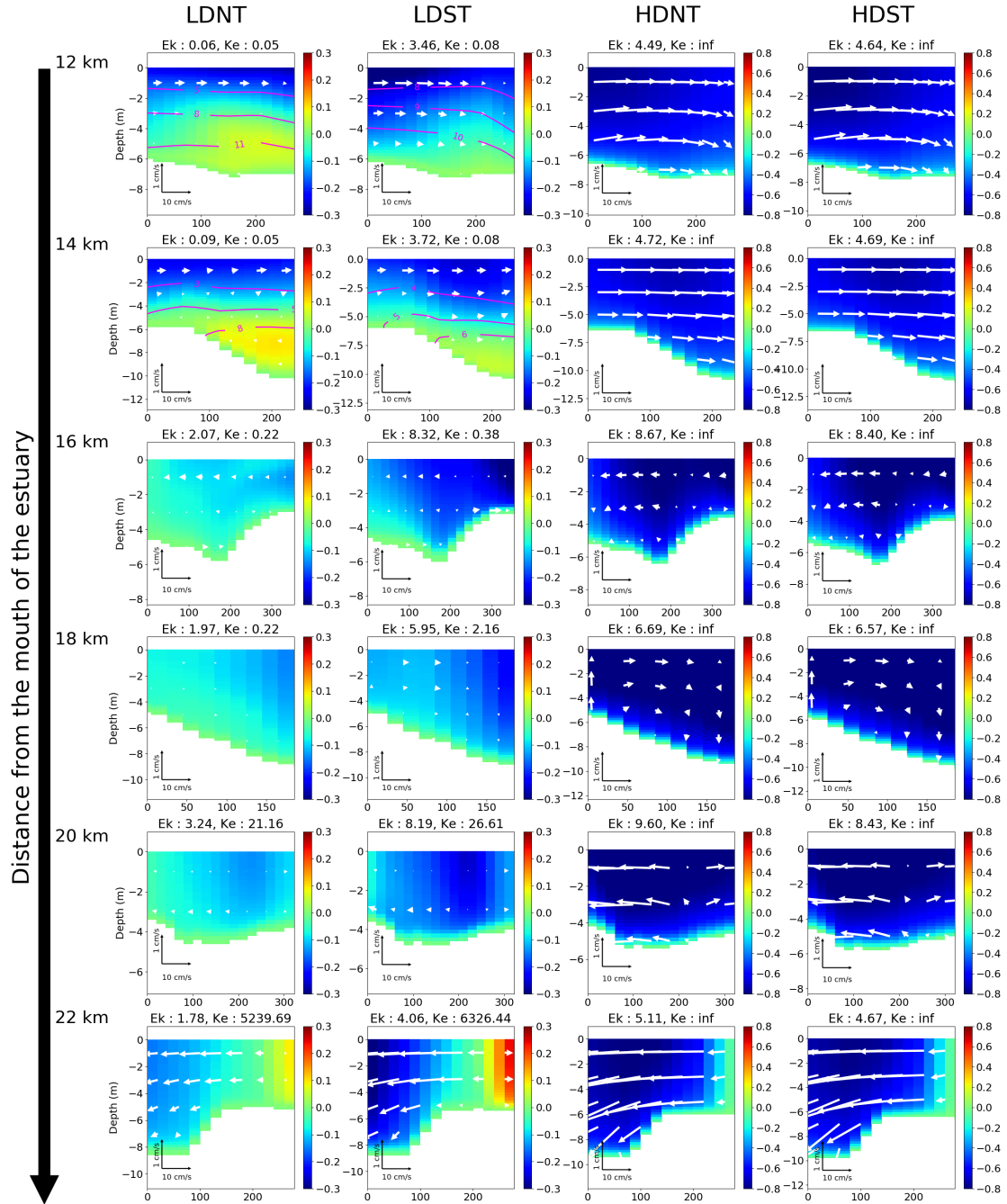


Figure 9: Cross-section of tidally-averaged along-channel velocity (in m/s on the colorbar) with positive values indicating inflow, tidally-averaged cross-channel velocity (white arrows) and tidally-averaged salinity (pink contour lines). From top to bottom cross-section correspond to the location of the red dot on Figure 6, respectively. To clarify the reading only one half of the cross-sections are represented on this figure (from 12 km to 22 km), the rest is presented in Figure 8. From left to right panel, each scenario is presented: low discharge and neap tide (LDNT), low discharge and spring tide (LDST), high discharge and neap tide (HDNT), and high discharge and spring tide (HDST). Tidally-averaged along-channel velocity colour scale is different for high discharge conditions than for low discharge conditions. The indicated Ekman (Ek) and Kelvin (Ke) numbers are discussed in section 5.1.

357 5. Discussion

358 The aim of this study was to expand our understanding of the variability of the subtidal flow
359 and the secondary circulation in a tidally-energetic meandering estuary. It has focused on the
360 major forcing switch driven by fortnightly cycles and seasonal discharge variations. The selected
361 study site enabled us to test the combined effects of complex morphology, strong vertical and
362 horizontal gradients and tidal mixing (Defontaine et al., 2019). A first overall observation of the
363 present study in the context of a narrow meandering estuary with time-dependent salt-wedge is the
364 striking variability of the residual circulation, with a complex 3D structure evolving with changes
365 in river discharge and tidal range but also showing a strong dependency on estuarine morphology.
366 The relative dominance of tidal and riverine forcing alternated along the fortnightly cycle during
367 both dry and wet seasons. Neap tides were characterised by a density-driven exchange flow up
368 to the saline intrusion limit. During the spring tides, the exchange flow is drastically weaker,
369 with a dominant outflow driven by advection and barotropic pressure gradients. Residual flows
370 are furthermore affected by the channel curvature and the cross-section bathymetry. Additional
371 discussion points are organised on the basis of two main topics with, first, the role played by the
372 estuarine morphology and, second, the possibility of predicting and classifying estuarine residual
373 circulation by dimensionless numbers. Finally, a short paragraph is dedicated to the limitations of
374 the tidally-averaged approach in such environments.

375 5.1. Influence of the estuarine morphology

376 It had been shown that the variation of estuarine morphology significantly affected the secondary
377 residual flows along the estuary. It also affected the along-channel residual flow in locations where
378 the section was locally reduced; the flow conservation induced a reinforcement of the residual
379 circulation by an increase of the advection. For instance, at the mouth of the estuary and 6
380 km upstream, the estuary width was reduced, both residual circulation and secondary circulation
381 were strengthened. The magnitude of the residual circulation can therefore be modulated by the
382 variations in width and depth along the channel, while the structure of residual flows is maintained.

383 Valle-Levinson (2008) showed to what extent the Ekman and Kelvin numbers are able to inves-
384 tigate the relative influence of basin width, friction and the Earth's rotation on the density-driven
385 exchange flow. The present analysis has been partly based on the Ekman (Ek) and Kelvin (Ke)
386 numbers presented in Figures 8 and 9. In the case of the Adour estuary, it was shown that the
387 estuary was density driven under neap tide condition up to the saline intrusion limit (i.e 16 and 2
388 km in the low/high river discharge scenarios, respectively). Estimation of both Ekman and Kelvin
389 numbers for those conditions have shown that the Adour estuary can be considered as narrow
390 ($Ke < 0.07$) and moderately frictional ($Ek < 0.35$). The Kelvin estimation indicated the Cori-
391 olis forcing was negligible in the Adour estuary, which was confirmed by the estimation of each
392 term of the momentum equation. The residual circulation pattern predicted by the Valle-Levinson
393 (2008) study for similar values of Ekman and Kelvin numbers was a vertically sheared exchange
394 with a clockwise secondary circulation cell. This pattern had been well reproduced by the present
395 simulations, with a further modification of the direction of rotation of the recirculation cell due to
396 meanders. Note that, as discussed later on, field observations would be necessary to validate the
397 numerical results.

398 The variations of the cross-section topography, from rectangle-like to a more triangular shaped,
 399 did not induce significant alteration of the along-channel pattern. Regarding the density driven
 400 flow (neap tide), such a weak influence was consistent with the Valle-Levinson (2008) study results
 401 for low to moderate friction cases. In other configurations (spring tide), advection and barotropic
 402 pressure gradient were prominent and the residual circulation followed the thalweg. Therefore cross-
 403 sectional topographic effects were not dominant in our context of a narrow meandering stratified
 404 estuary.

405 5.2. Tidal mixing and stratification parameter space

406 Geyer and MacCready (2014) presented a new classification scheme based on two parameters:
 407 the freshwater Froude number and the Mixing number. The freshwater Froude number Fr_f rep-
 408 represents the net velocity due to river flow scaled by the maximum possible frontal propagation
 409 speed: $Fr_f = U_r / (\beta g s_{ocean} H)^{1/2}$, where $U_r = Q_r / S$ is freshwater velocity approximated as the
 410 ratio of the river flow (Q_r) and the area of the section (S), $\beta = 7.710^4$ is the coefficient of saline
 411 contraction, $g = 9.81 m/s^2$ is the acceleration due to gravity, $s_{ocean} = 35$ is the ocean salinity
 412 and H is the mean water depth. The Mixing number M provides a scaling of the tidal velocity:
 413 $M = \sqrt{(C_d U_t^2) / (\omega N_0 H^2)}$, where U_t is the tidal velocity, $C_D = 0.003$ is the bottom drag coef-
 414 ficient, $\omega = 1/T_{M2}$ is the tidal frequency and $N_0 = (\beta g s_{ocean} / H)^{1/2}$ is the buoyancy frequency.
 415 This $M - Fr_f$ parameter space aims to investigate the respective contribution of tidal mixing and
 416 stratification and therefore to provide a classification diagram for estuaries as depicted in Figure
 417 10. Estuarine circulation regimes are separated by a "diagonal mixing line" (red thick line in Fig.
 418 10) which is assumed to segregate the permanent stratified estuaries from those in which mixing
 419 can be spread over the whole water column within a tidal cycle (Geyer and MacCready, 2014).
 420 Such a separation was established based on experimental data from the San Francisco Bay (Stacey
 421 et al., 2001) and a series of numerical results (Cheng et al., 2010; Burchard et al., 2011). Using
 422 typical values obtained 6 kilometres from the mouth of the estuary for nine simulations, the four
 423 simulations presented above and five additional simulations with medium river discharge (MD :
 424 $Q_{Adour} = 300.0$ and $Q_{Nive} = 60.0$) and medium tidal range (MT : 3.10 m), the dimensionless
 425 parameters obtained range from 0.03 to 0.44 for the freshwater Froude and from 0.36 to 1.2 for the
 426 Mixing parameter. These values are slightly higher than those estimated with experimental data
 427 (Defontaine et al., 2019), due to more contrasted hydrological conditions. Parameters estimated
 428 for the nine idealized cases are indicated by dots in Figure 10, where colours are related to tidal
 429 range: neap tides in black, spring tides in red and mean tidal range in blue. The diagonal mixing
 430 line segregates properly the different tidal conditions, with the red dots (i.e. spring tides) on the
 431 right side and the black dots (i.e. neap tides) on the left side, while the blue dots are spread along
 432 the diagonal. The residual along-channel velocity profiles in the thalweg corresponding to these
 433 nine simulations are presented in Figure 11, where the colours still correspond to the tidal range
 434 and the line style to the river input. Broadly speaking, neap tides are associated with an exchange
 435 flow and spring tides with an outflow, while for medium tidal range the structure of residual flows
 436 oscillates between the two patterns. In the case of a very high river flow, the salt-wedge is not able
 437 to reach the point at 6 km from the mouth of the estuary where the data were extracted, therefore
 438 the residual flow displays a classical logarithmic profile (Fig. 6 c and e). Despite the difference
 439 in morphological and hydrodynamic conditions between the Adour estuary and the cases used to

440 build the regime diagram and the mixing line (Stacey et al., 2001; Cheng et al., 2010; Burchard
 441 et al., 2011), the proposed $M - Fr_f$ approach seems to be fairly appropriate to diagnose and to
 442 predict the structure of residual flows, with exchange flow on the left side of the diagonal line and
 443 flow out of the estuary over the whole water column on the right side. The further we are from the
 444 diagonal line, the clearer the trend is. However, in less contrasted conditions, the forcing seem to
 445 be balanced and residual flows can be influenced by additional secondary parameters.

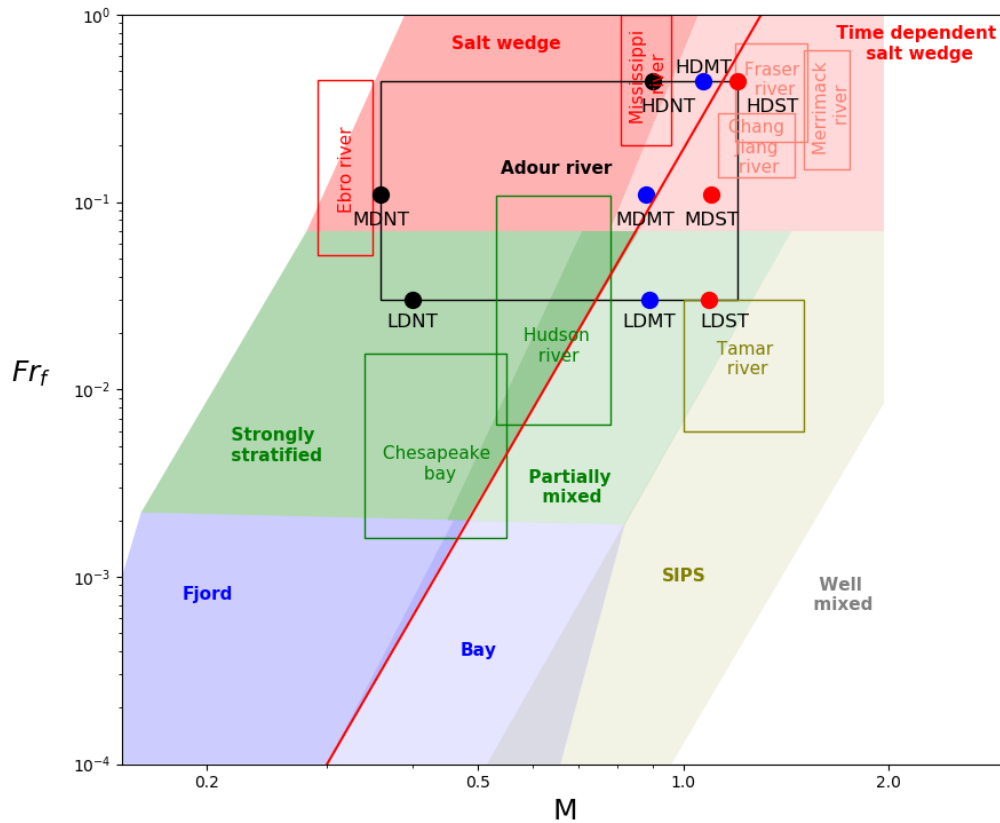


Figure 10: Estuarine classification based on the freshwater Froude number and Mixing number, adapted from Fig. 6 of Geyer and MacCready (2014). The black rectangle represents the Adour river estuary based on simulation results. The colour dots indicate the values for the nine simulation runs and colours are related to tidal range: neap tides in black, spring tides in red and mean tidal range in blue.

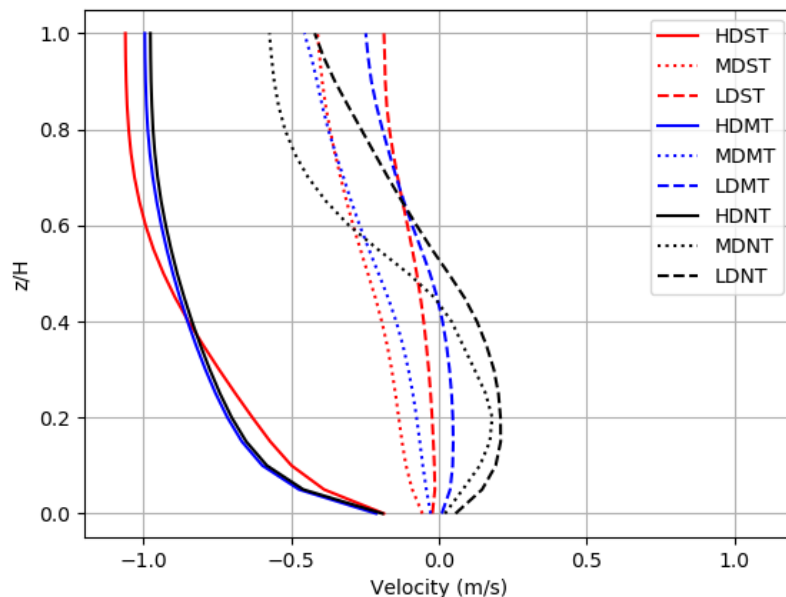


Figure 11: Residual along-channel velocity simulated 6 km from the mouth of the estuary. Positive values indicate water flowing into the estuary.

446 *5.3. Study limitations*

447 The use of tidally-averaged parameters when studying a time-dependent salt-wedge estuary can
 448 be questioned. In such estuaries, the vigorous tidal forcing can break down the salt-wedge structure
 449 during the ebb and completely destratify the water column. The salt-wedge may even be completely
 450 flushed out during the ebb tide, resulting in a homogeneous fresh water estuary. As the longitudinal
 451 density gradient is strongly variable throughout the tidal cycle, the tidally-averaged parameters are
 452 representative of neither the ebb structure nor the flood structure. These limitations should be
 453 taken into consideration when using dimensionless parameters for classification and more generally
 454 when inferring more general water and tracer dispersion trends from tidally-averaged circulation
 455 patterns.

456 Numerical models, even if widely used for estuarine study, are developed based on hypothesis
 457 and approximations due to a lack of information or to facilitate the calculation and reduce the
 458 calculation time. In addition, numerical models add computational artefacts such as numerical
 459 diffusion. Even with satisfying calibration and validation, some under/overestimation of physical
 460 processes may appear. In our model, an overestimation of the exchange flow is observed on the
 461 second neap tide period in Figure 5. This could be due to an underestimation of turbulent mixing
 462 by the turbulence model. Furthermore, the secondary circulation, as well as the lateral variation
 463 of along-channel residual flows simulated by the models were not fully validated by observations.
 464 Despite their costs, additional in-situ high resolution experimental campaigns should be envisioned
 465 to further refine the model validation.

466 6. Conclusion

467 A 3D numerical model was developed to study the response of the residual flow structure to
468 the variations of tidal and river flow forcing in a meandering estuary. The numerical model was
469 calibrated and validated with experimental data. A satisfactory agreement was observed on water
470 elevation, velocity, salinity field data and residual circulation.

471 The numerical results show that two distinct residual flow patterns can be identified over the
472 course of a fortnightly cycle: a density-driven exchange flow and an outflow. The first pattern is
473 exhibited during neap tides and more pronounced during high discharge conditions, and associated
474 with a momentum balance dominance by baroclinic and barotropic pressure gradients. During
475 spring tides, the baroclinic pressure gradient is overwhelmed by the barotropic pressure gradient and
476 advection, resulting in an outflow. The pattern of residual flows varied with the tidal range, while
477 the magnitude of residual flows is governed by the river discharge, with a residual circulation twice
478 as high during high river discharge as during low river discharge. A secondary cross-channel residual
479 flow was observed at the selected transects. It is affected by the estuarine morphology (including the
480 local curvature and constriction) and the along-channel residual circulation. Nevertheless, cross-
481 sectional topographic effects are not dominant in a narrow stratified estuary. Finally, the Geyer
482 and MacCready (2014) classification scheme based on the $M - Fr_f$ regime diagram was successfully
483 applied to distinguish the residual flow structure. The related mixing line was able to discriminate
484 exchange flow and outflow conditions in the estuarine residual circulation.

485 7. Acknowledgements

486 This study was supported by the BIGCEES project (E2S UPPA). Authors would like to express
487 their gratitude to Philippe Maron for his advice and assistance with numerical work.

488 References

- 489 Alahmed, S., Ross, L., Sottolichio, A., 2021. The role of advection and density gradients in driving
490 the residual circulation along a macrotidal and convergent estuary with non-idealized geometry.
491 Continental Shelf Research 212, 104295.
- 492 Bellafont, F., Morichon, D., Roeber, V., André, G., Abadie, S., 2018. Infragravity period oscillations
493 in a channel harbor near a river mouth. Coastal Engineering Proceedings 1 (36), 8.
- 494 Burchard, H., Hetland, R. D., 2010. Quantifying the contributions of tidal straining and grav-
495 itational circulation to residual circulation in periodically stratified tidal estuaries. Journal of
496 Physical Oceanography 40 (6), 1243–1262.
- 497 Burchard, H., Hetland, R. D., Schulz, E., Schuttelaars, H. M., 2011. Drivers of residual estuarine
498 circulation in tidally energetic estuaries: Straight and irrotational channels with parabolic cross
499 section. Journal of Physical Oceanography 41 (3), 548–570.
- 500 Caceres, M., Valle-Levinson, A., Atkinson, L., 2003. Observations of cross-channel structure of flow
501 in an energetic tidal channel. Journal of Geophysical Research: Oceans 108 (C4).

- 502 Chant, R. J., 2002. Secondary circulation in a region of flow curvature: Relationship with tidal
503 forcing and river discharge. *Journal of Geophysical Research: Oceans* 107 (C9), 14–1.
- 504 Chant, R. J., Sommerfield, C. K., Talke, S. A., 2018. Impact of channel deepening on tidal and
505 gravitational circulation in a highly engineered estuarine basin. *Estuaries and coasts* 41 (6),
506 1587–1600.
- 507 Chant, R. J., Wilson, R. E., 1997. Secondary circulation in a highly stratified estuary. *Journal of*
508 *Geophysical Research: Oceans* 102 (C10), 23207–23215.
- 509 Chatwin, P., 1976. Some remarks on the maintenance of the salinity distribution in estuaries.
510 *Estuarine and Coastal Marine Science* 4 (5), 555–566.
- 511 Chawla, A., Jay, D. A., Baptista, A. M., Wilkin, M., Seaton, C., 2008. Seasonal variability and
512 estuary-shelf interactions in circulation dynamics of a river-dominated estuary. *Estuaries and*
513 *Coasts* 31 (2), 269–288.
- 514 Cheng, P., Valle-Levinson, A., De Swart, H. E., 2010. Residual currents induced by asymmetric tidal
515 mixing in weakly stratified narrow estuaries. *Journal of physical oceanography* 40 (9), 2135–2147.
- 516 Defontaine, S., 2019. Saline structure circulation and suspended sediment transport in a channelized
517 salt-wedge estuary : the adour river estuary. Ph.D. thesis, Université de PAu et des Pays de
518 l’Adour.
- 519 Defontaine, S., Sous, D., Morichon, D., Verney, R., Monperrus, M., 2019. Hydrodynamics and spm
520 transport in an engineered tidal estuary: the adour river (france). *Estuarine, Coastal and Shelf*
521 *Science*.
- 522 Geyer, W., Cannon, G., 1982. Sill processes related to deep water renewal in a fjord. *Journal of*
523 *Geophysical Research: Oceans* 87 (C10), 7985–7996.
- 524 Geyer, W. R., MacCready, P., 2014. The estuarine circulation. *Annual review of fluid mechanics*
525 46, 175–197.
- 526 Geyer, W. R., Trowbridge, J. H., Bowen, M. M., 2000. The dynamics of a partially mixed estuary.
527 *Journal of Physical oceanography* 30 (8), 2035–2048.
- 528 Hansen, D. V., Rattray, M., 1966. New dimensions in estuary classification. *Limnology and Oceanog-*
529 *raphy* 11 (3), 319–326.
- 530 Hervouet, J.-M., 2007. *Hydrodynamics of free surface flows: modelling with the finite element*
531 *method*. Wiley Online Library.
- 532 Jay, D. A., Smith, J. D., 1990. Residual circulation in shallow estuaries: 1. highly stratified, narrow
533 estuaries. *Journal of Geophysical Research: Oceans* 95 (C1), 711–731.
- 534 Kim, Y. H., Voulgaris, G., 2008. Lateral circulation and suspended sediment transport in a curved
535 estuarine channel: Winyah bay, sc, usa. *Journal of Geophysical Research: Oceans* 113 (C9).
- 536 Lerczak, J. A., Geyer, R. W., 2004. Modeling the lateral circulation in straight, stratified estuaries.
537 *Journal of Physical Oceanography* 34 (6), 1410–1428.

- 538 Li, C., O'Donnell, J., 2005. The effect of channel length on the residual circulation in tidally
539 dominated channels. *Journal of Physical Oceanography* 35 (10), 1826–1840.
- 540 Noble, M. A., Schroeder, W. W., Wiseman Jr, W. J., Ryan, H. F., Gelfenbaum, G., 1996. Subtidal
541 circulation patterns in a shallow, highly stratified estuary: Mobile bay, alabama. *Journal of*
542 *Geophysical Research: Oceans* 101 (C11), 25689–25703.
- 543 Peng, S.-H., Davidson, L., Holmberg, S., 1996. The two-equations turbulence k - ω model applied to
544 recirculating ventilation flows. *Rept* 96 (13), 276–285.
- 545 Pritchard, D. W., 1952. Salinity distribution and circulation in the chesapeake bay estuarine system.
546 *Journal of Marine Research* 11 (2), 106–123.
- 547 Ralston, D. K., Geyer, W. R., Lerczak, J. A., 2008. Subtidal salinity and velocity in the hudson
548 river estuary: Observations and modeling. *Journal of Physical Oceanography* 38 (4), 753–770.
- 549 Ross, L., Valle-Levinson, A., Sottolichio, A., Huybrechts, N., 2017. Lateral variability of subtidal
550 flow at the mid-reaches of a macrotidal estuary. *Journal of Geophysical Research: Oceans* 122 (9),
551 7651–7673.
- 552 Scully, M. E., Geyer, W. R., Lerczak, J. A., 2009. The influence of lateral advection on the residual
553 estuarine circulation: A numerical modeling study of the hudson river estuary. *Journal of Physical*
554 *Oceanography* 39 (1), 107–124.
- 555 Stacey, M. T., Burau, J. R., Monismith, S. G., 2001. Creation of residual flows in a partially
556 stratified estuary. *Journal of Geophysical Research: Oceans* 106 (C8), 17013–17037.
- 557 Tenorio-Fernandez, L., Valle-Levinson, A., Gomez-Valdes, J., 2018. Subtidal hydrodynamics in a
558 tropical lagoon: A dimensionless numbers approach. *Estuarine, Coastal and Shelf Science* 200,
559 449–459.
- 560 Valle-Levinson, A., 2008. Density-driven exchange flow in terms of the kelvin and ekman numbers.
561 *Journal of Geophysical Research: Oceans* 113 (C4).
- 562 Valle-Levinson, A., De Velasco, G. G., Trasviña, A., Souza, A. J., Durazo, R., Mehta, A. J., 2009.
563 Residual exchange flows in subtropical estuaries. *Estuaries and coasts* 32 (1), 54–67.
- 564 Valle-Levinson, A., Schettini, C. A., 2016. Fortnightly switching of residual flow drivers in a tropical
565 semiarid estuary. *Estuarine, Coastal and Shelf Science* 169, 46–55.
- 566 Wilcox, D. C., 1988. Reassessment of the scale-determining equation for advanced turbulence mod-
567 els. *AIAA journal* 26 (11), 1299–1310.
- 568 Wong, K.-C., 1994. On the nature of transverse variability in a coastal plain estuary. *Journal of*
569 *Geophysical Research: Oceans* 99 (C7), 14209–14222.
- 570 Wong, K.-C., Garvine, R. W., 1984. Observations of wind-induced, subtidal variability in the
571 delaware estuary. *Journal of Geophysical Research: Oceans* 89 (C6), 10589–10597.